Science Advances
AAAS

Supplementary Materials for

Tissue-adhesive hydrogel–MXene biosensor for in situ intraoral TNF-α detection

Tsz Hung Wong *et al.*

Corresponding author: Chenglin Wu, chenglinwu@tamu.edu; Shaoting Lin, linshaot@msu.edu

Sci. Adv. **12**, eady9180 (2026)
DOI: 10.1126/sciadv.ady9180

The PDF file includes:

Supplementary Text
Figs. S1 to S28
Tables S1 and S2
Legends for movies S1 to S3

Other Supplementary Material for this manuscript includes the following:

Movies S1 to S3

Supplementary Text

Finite element simulation of TAHM biosensor with tissue-adhesive hydrogel on gingival surface

Calculation of the energy release rate at the TAHM biosensor/tissue-adhesive hydrogel interface (with tissue-adhesive hydrogel). All finite element simulations were conducted using ABAQUS/Explicit. We began with the setup of the TAHM biosensor attached to a gingiva surface using the tissue-adhesive hydrogel (**fig. S16A, B**). Firstly, the deformation of the TAHM biosensor, sealed by a tissue-adhesive hydrogel and attached to the gingival surface, was simulated along with the crack propagation at the TAHM biosensor/tissue-adhesive hydrogel interface. The TAHM biosensor and the selective-permeable hydrogel both measured 20 mm × 10 mm × 1 mm (length × width × thickness), while the tissue-adhesive hydrogel measured 20 mm × 20 mm × 3 mm, and the gingiva measured 20 mm × 20 mm × 10 mm. Two cracks, each with dimensions of 20 mm × 1 mm × 1 mm, were introduced at both edges of the interface, resulting in a crack area of $\Delta A_{\mathrm{s-TAH}} = 40\ \mathrm{mm}^2$.

Secondly, the first-order Ogden hyperelastic model was employed to characterize the large deformation behavior of the soft materials within the structure. The strain energy density function for the model is expressed as:

$$W = 2\mu_1/\alpha_1^2(\lambda_1^{\alpha_1} + \lambda_2^{\alpha_1} + \lambda_3^{\alpha_1} - 3) \quad (1)$$

Here, W represents the strain energy density, while $\lambda_1, \lambda_2, \lambda_3$ denote the three principal stretch ratios. The parameter μ_1 corresponds to the shear modulus, and α_1 is a material constant. For soft materials including gingiva, SPH membrane, and TAH patch, the material parameters μ_1 and α_1 were determined by fitting experimental data (as shown in **fig. S15**). The summarized values are as follow: Gingiva (μ_1 = 164.92 kPa, α_1 = 9.3675), SPH membrane (μ_1 = 14.66 kPa, α_1 = 4.43), and TAH patch (μ_1 = 137.4 kPa, α_1 = 1.47). The sensor exhibits elastic deformation, characterized by a Young's modulus of 100 GPa and a Poisson's ratio of 0.17. After the sensor, selective-permeable hydrogel, tissue-adhesive hydrogel, and gingiva were tied, the gingiva was subjected to loading along its width direction at a constant velocity of 0.2 mm/s for 50 seconds, resulting in a stretch ratio of $\lambda = 1.5$. The model employed 3D-stress 8-node linear elements. Analyses were conducted for both the model with two cracks and the model without cracks to determine the energy release rate, $G_{\mathrm{s-TAH}}$.

$$G_{s-\mathrm{TAH}} = \frac{-\Delta U}{\Delta A_{\mathrm{s-TAH}}} \quad (2)$$

where $\Delta U = U_{\text{with crack}} - U_{\text{without crack}}$. $U_{\text{without crack}}$ represents the strain energy of the entire model without cracks (**fig. S16C**), and $U_{\text{with crack}}$ denotes the strain energy of the entire model with cracks presenting at the interface between the tissue-adhesive hydrogel and the sensor (**fig. S16 D, E**).

Calculation of the energy release rate at the gingiva/tissue-adhesive hydrogel interface (with tissue-adhesive hydrogel). The same models with identical geometric and material parameters were utilized to calculate the energy release rate where two identical cracks were introduced at the

interface between the gingiva and the tissue-adhesive hydrogel (**fig. S16F**). As before, the first-order Ogden hyperelastic model was employed to characterize the large deformation behavior of the soft materials in the structure, with the strain energy density function and material fitting parameters provided in table S1. Both models, with and without cracks, were analyzed to determine the energy release rate, $G_{\mathrm{g-TAH}}$.

$$G_{g-\mathrm{TAH}} = \frac{-\Delta U}{\Delta A_{\mathrm{g-TAH}}} \tag{3}$$

where $\Delta U = U_{\text{with crack}} - U_{\text{without crack}}$. $U_{\text{without crack}}$ represents the strain energy of the entire model without cracks, and $U_{\text{with crack}}$ denotes the strain energy of the entire model with cracks present at the interface between the tissue-adhesive hydrogel and the gingiva (**fig. S16G**, **H**).

Calculation of the energy release rate at the gingiva/selective-permeable hydrogel interface (with tissue-adhesive hydrogel). The same models with identical geometric and material parameters were utilized to calculate the energy release rate where two identical cracks were introduced at the interface between the gingiva and the selective-permeable hydrogel (**fig. S16I**).As before, the first-order Ogden hyperelastic model was employed to characterize the large deformation behavior of the soft materials in the structure, with the strain energy density function and material fitting parameters provided in table S1. Both models, with and without cracks, were analyzed to determine the energy release rate,$G_{\mathrm{g-SPH}}$.

$$G_{g-SPH} = \frac{-\Delta U}{\Delta A_{\mathrm{g-SPH}}} \tag{4}$$

where $\Delta U = U_{\text{with crack}} - U_{\text{without crack}}$. $U_{\text{without crack}}$ represents the strain energy of the entire model without cracks, and $U_{\text{with crack}}$ denotes the strain energy of the entire model with cracks present at the interface between the tissue-adhesive hydrogel and the gingiva. (**fig. S16J**, **K**).

Calculation of the energy release rate at the TAHM biosensor/selective-permeable hydrogel interface (with tissue-adhesive hydrogel). The same models with identical geometric and material parameters were utilized to calculate the energy release rate where two identical cracks were introduced at the interface between the TAHM biosensor and the selective-permeable hydrogel (**fig. S16L**). As before, the first-order Ogden hyperelastic model was employed to characterize the large deformation behavior of the soft materials in the structure, with the strain energy density function and material fitting parameters provided in **table S1**. Both models, with and without cracks, were analyzed to determine the energy release rate $G_{\mathrm{s-SPH}}$.

$$G_{s-SPH} = \frac{-\Delta U}{\Delta A_{\mathrm{s-SPH}}} \tag{5}$$

where $\Delta U = U_{\text{with crack}} - U_{\text{without crack}}$. $U_{\text{without crack}}$ represents the strain energy of the entire model without cracks, and $U_{\text{with crack}}$ denotes the strain energy of the entire model with cracks

present at the interface between the TAHM biosensor and the selective-permeable hydrogel (**fig. S16M**, **N**).

The strain condition of a TAHM biosensor (with a tissue-adhesive hydrogel) without any cracks was also examined using the previously described methodology. Additionally, **movie S1** demonstrates the strain distribution of a TAHM biosensor with cracks at different interfaces.

Finite element simulation of the TAHM biosensor attached to the gingiva without a tissue-adhesive hydrogel

Calculation of the energy release rate at the TAHM biosensor/selective-permeable hydrogel interface (without tissue-adhesive hydrogel). Simulations were conducted for a TAHM biosensor and a selective-permeable hydrogel directly attached to the gingiva (without the use of tissue-adhesive hydrogel) (**fig. S17A**, **C**). Two cracks, each with dimensions of 20 mm × 2 mm × 1 mm, were introduced at both edges of the interface, resulting in a crack area of $\Delta A_{\mathrm{s-TAH}} = 80\ \mathrm{mm}^2$. The remaining simulations were conducted using the same methodology as previously outlined in "*Calculation of the energy release rate at the TAHM biosensor/selective-permeable hydrogel interface (with tissue-adhesive hydrogel)*" (**fig. S17B**, **D**, **E**).

Calculation of the energy release rate at the gingiva/selective-permeable hydrogel interface (without tissue-adhesive hydrogel). Simulations were conducted for a selective-permeable hydrogel directly attached to the gingiva (without the use of tissue-adhesive hydrogel) (**fig. S17F**). Two cracks, each with dimensions of 40 mm × 4 mm × 1 mm, were introduced at both edges of the interface, resulting in a crack area of $\Delta A_{\mathrm{s-TAH}} = 160\ \mathrm{mm}^2$. The remaining simulations were conducted using the same methodology as previously outlined in "*Calculation of the energy release rate at the gingiva/selective-permeable hydrogel interface (with tissue-adhesive hydrogel)*" (**fig. S17G**, **H**).

The strain distribution of a TAHM biosensor (without tissue-adhesive hydrogel) without any crack was also examined by adopting the previous methodology.

Finite element simulation of the TAMH biosensor attached to the tissue-adhesive hydrogel under stretching.

Simulation of a TAHM biosensor attached to a glass substrate and directly patched onto the tissue-adhesive hydrogel was conducted using the same methodology outlined in "*Finite element simulation of TAHM biosensor with tissue-adhesive hydrogel on gingival surface.*" The TAHM biosensor has dimensions of 4 mm × 4 mm × 1 mm, while the tissue-adhesive measures 8 mm × 20 mm × 1 mm.

The first-order Ogden hyperelastic model and material parameters used were identical to those outlined in "*Calculation of the energy release rate at the TAHM biosensor/tissue-adhesive hydrogel interface (with tissue-adhesive hydrogel).*" The sensor, mounted on a piece of glass, deforms elastically with a Young's modulus of 100 GPa and a Poisson's ratio of 0.17. The interfaces between the sensor and the tissue-adhesive hydrogel were tied. The tissue-adhesive hydrogel was loaded along its length at a constant velocity of 0.2 mm/s for a duration of 100

seconds, resulting in a stretch ratio of $\lambda = 2$. The model employed 3D-stress 8-node linear elements. During the deformation of the tissue-adhesive hydrogel, the sensor patched onto the hydrogel experienced minimal deformation, demonstrating the protective role of the tissue-adhesive hydrogel in safeguarding the sensor during stretching.

The strain condition of a TAHM biosensor (without a tissue-adhesive hydrogel) without any cracks was also examined using the previously described methodology. Additionally, **movie S2** demonstrates the strain condition of a TAHM biosensor with cracks at different interfaces.

Calculation of the average mesh size of selective-permeable hydrogel membrane.

The calculation of the average mesh size of SPH refers to the following equation:

$$R = \sqrt{N}b \tag{6}$$

The polymer network is modeled as freely rotating chain segments composed of N rigid links of equal length b, with the end-to-end segment length R representing the mesh size. Based on the formulation described in the "*Synthesis of the Selective-Permeable Hydrogel Membrane*" section in Materials and Methods, the average mesh size of the resulting SPH is approximately 6.9 nm. By varying the concentration of the crosslinker MBAA, the mesh size can be readily tuned. For instance, SPH samples with average mesh sizes of approximately 3.9 nm and 9.7 nm were synthesized by incorporating 3 mL and 0.5 mL of MBAA, respectively, into the same base formulation.

Calculation of diffusivity from FRAP results.

To extract diffusivity parameters, the normalized intensity recovery curves were fitted using the Soumpasis equation, which models diffusion-driven recovery dynamics. The normalized intensity $\bar{I}(t)$ is defined as:

$$\bar{I}(t) = \frac{I(t) - I(0)}{I(0^-) - I(0)} \tag{7}$$

where $I(t)$ is the fluorescence intensity is measured at time t, $I(0)$ is the intensity immediately after bleaching, and $I(0^-)$ is the initial intensity.

The theoretical model used for fitting is:

$$\bar{I}(t) = e^{-\omega^2/2Dt}\left[B_0\left(\frac{\omega^2}{2D}\right)^2 + B_1\left(\frac{\omega^2}{2D}\right)\right] \tag{8}$$

where ω is the radius of the bleached spot, D is the diffusion coefficient, and B_0 and B_1 are the modified Bessel functions of the first kind of order 0 and 1, respectively. The fitting procedure minimizes the mean square error between the experimental data and the model, allowing for accurate determination of the diffusion coefficient, D.

The mobile fraction was calculated with the following equation.

$$\text{Mobile fraction} = \frac{I(\infty) - I(0)}{I(0^-) - I(0)} \tag{9}$$

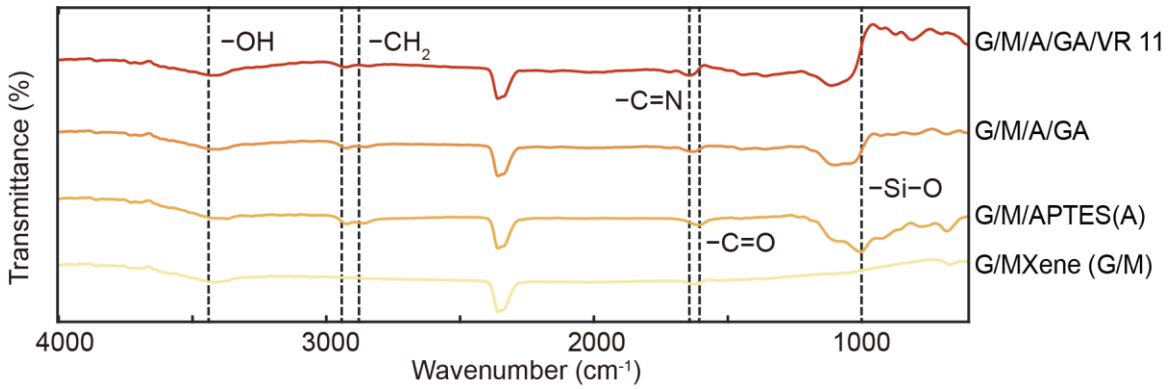


Fig. S1. **Fourier-transform infrared (FTIR) spectra confirming the stepwise surface functionalization of the graphene/MXene sensing probe.** Characteristic peaks corresponding to –OH (~3420 cm^{-1}), –C=O (~1575 cm^{-1}), –CH_2 (~2900 cm^{-1}), Si–O (~1000 cm^{-1}), and C=N (~1690 cm^{-1}) are observed, indicating successful sequential modification with APTES, glutaraldehyde (GA), and VR11 aptamer. The progressive appearance of these peaks validates the chemical bonding and functional group incorporation throughout the surface modification process.

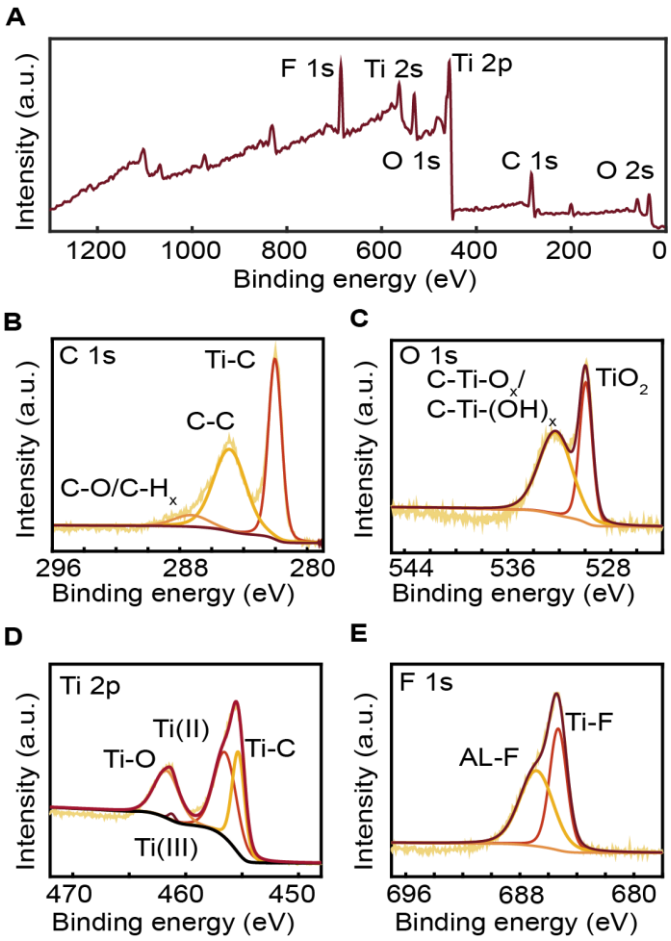


Fig. S2. **X-ray Photoelectron Spectroscopy (XPS) analysis of etched MXene reveals its elemental composition and surface chemical states, confirming the successful transformation from the precursor MAX phase to MXene.** (**A**) Survey spectrum showing the presence of Ti, C, O, and F, indicating effective etching and surface modification. (**B**) High-resolution C 1s spectrum demonstrating C–Ti bonding and surface functionalities such as C–O and C–H. (**C**) O 1s spectrum indicating the presence of C-Ti-Ox and C-Ti-(OH)x groups, and TiO_2, reflecting oxygen incorporation during the etching process. (**D**) Ti 2p spectrum showing characteristic peaks of Ti–C, Ti(II), Ti(III), and Ti–O, revealing mixed valence states of titanium. (**E**) F 1s spectrum highlighting surface fluorination resulting from fluoride-based etching chemistry.

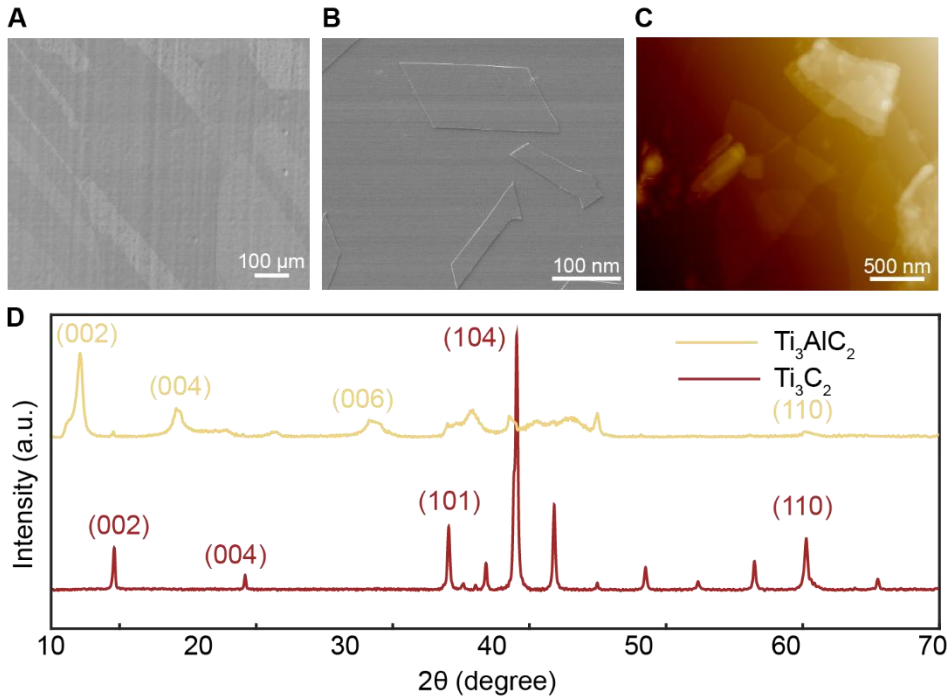


Fig. S3. **Morphological and structural characterizations of monolayer graphene and synthesized Ti_3C_2 MXene.** (**A**) Scanning electron microscopy (SEM) image of monolayer graphene, displaying a continuous and smooth surface, indicative of uniform film quality. (**B**) SEM image of Ti_3C_2 MXene flakes, revealing an accordion-like layered structure characteristic of etched MXene with sheet-like morphology. (**C**) Atomic force microscopy (AFM) image of exfoliated MXene flakes, providing detailed topographical information and confirming the nanosheet thickness. (**D**) X-ray diffraction (XRD) patterns of the precursor MAX phase and the resulting Ti_3C_2 MXene. The disappearance of the (104) peak and the downshift of the (002) reflection indicate successful etching of Al layers and the formation of a layered MXene structure with enlarged interlayer spacing.

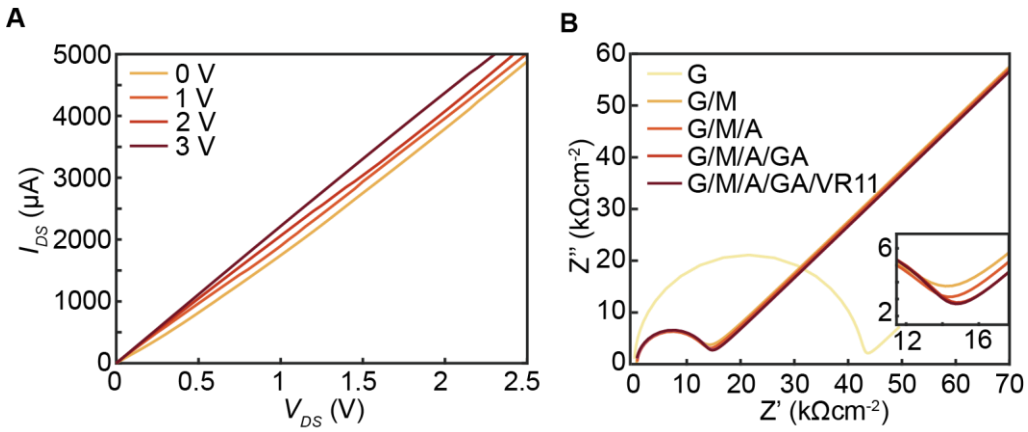


Fig. S4. **Electrical characterization of the G/MXene-based FET sensor before and after surface functionalization.** (A) The I_{DS}–V_{DS} characteristics of the functionalized FET sensor exhibit linear conduction behavior across all measurements, confirming ohmic contact and stable operation in the linear regime. The slope of the curves increases with increasing gate voltage (V_G), indicating enhanced carrier injection and channel conductance. (**B**) Electrochemical impedance spectroscopy (EIS) Nyquist plots of the FET sensor before and after MXene integration and surface functionalization. The pronounced reduction in the semicircle diameter following MXene incorporation reflects improved charge transfer efficiency and reduced channel resistance, attributable to the high conductivity and electron mobility of MXene.

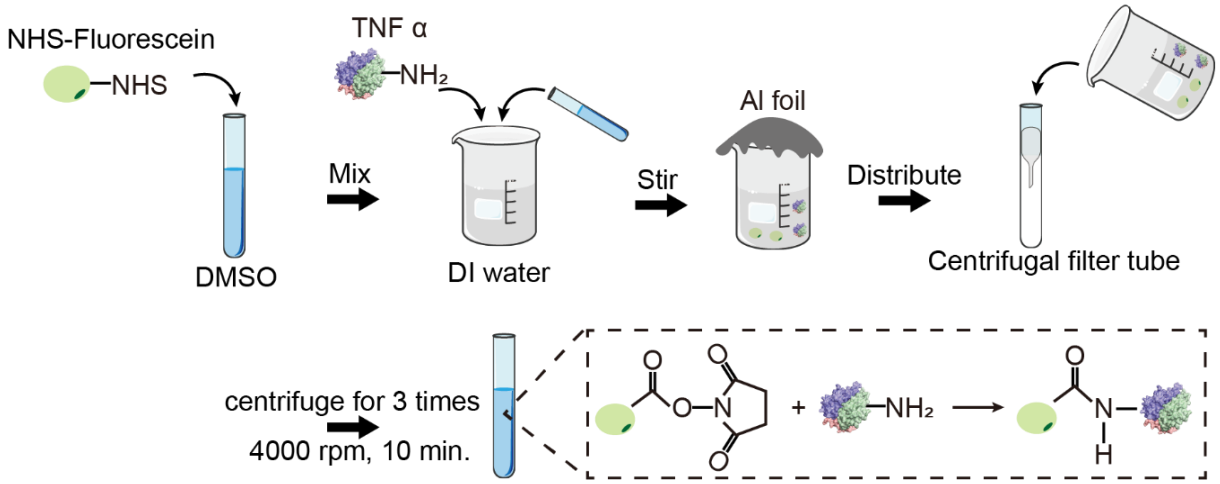


Fig. S5. Schematic illustration of the synthesis procedure for labeling TNF-α with NHS-Fluorescein. The process includes NHS-Fluorescein dissolution, conjugation with TNF-α via amine-reactive chemistry, purification using centrifugal filtration to remove unreacted dye, and storage under light-protected, low-temperature conditions. This labeling enables subsequent fluorescence-based analysis of molecules diffusion in FRAP experiments.

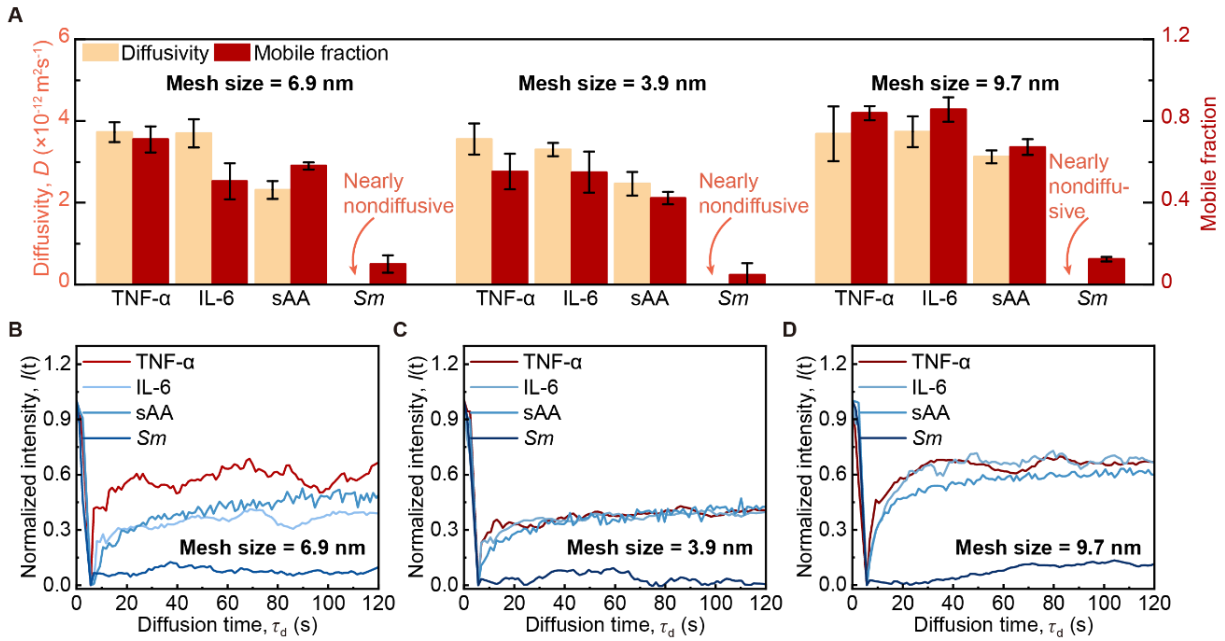


Fig. S6. Fluorescence recovery after photobleaching (FRAP) analysis of target TNF-α and non-target biomolecules diffusing through selective-permeable hydrogel membranes. (**A**) Summary of calculated diffusivity and mobile fraction values for target TNF-α and non-target biomolecules including IL-6, human salivary amylase (sAA), and Streptococcus mutans (*Sm*). (**B-D**) Normalized fluorescence recovery curves of various biomolecules over time in hydrogels with mesh sizes of approximately 6.9 nm (**B**), 3.9 nm (**C**), and 9.7 nm (**D**). Data in (**B**, **C**, and **D**) represent mean ± standard deviation ($n = 4$).

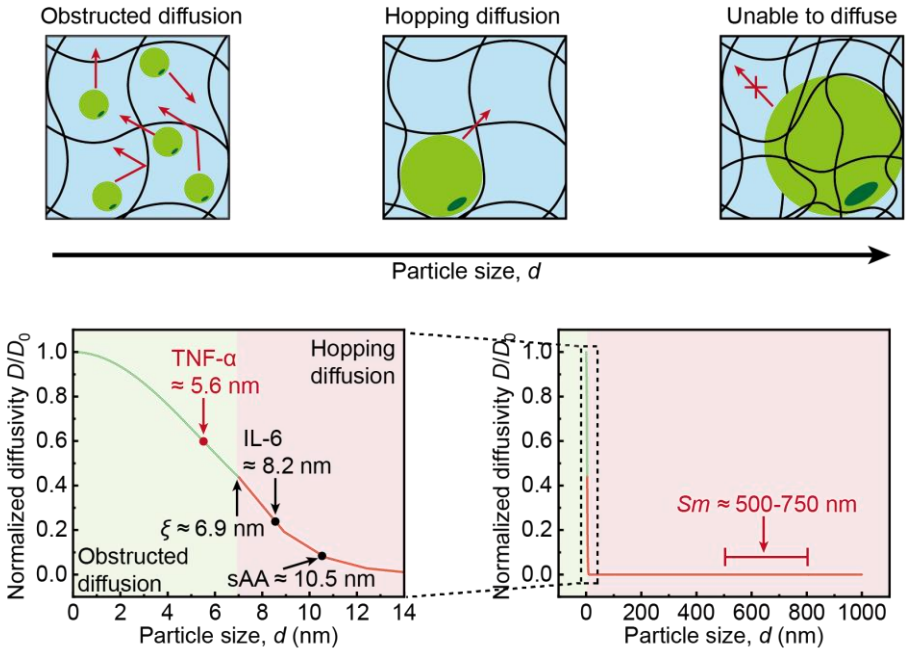


Fig. S7. Diffusion behaviors of particles with various sizes within a polymer matrix. (**A**) Schematic illustrations showing the diffusion of particles with different sizes within polymer networks. (**B**) Normalized theoretical diffusivity as a function of particle size.

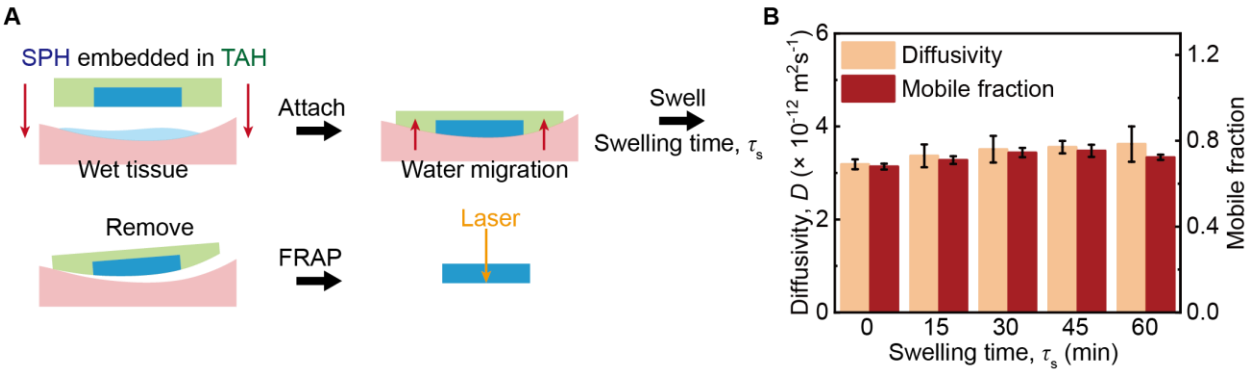


Fig. S8. Characterization of the effect of SPH swelling on its permeability. (**A**) Schematic illustration of the experimental setup. (**B**) The diffusivity and mobile fraction of TNF-α within the SPH (with a mesh size approximately 6.9 nm) after different swelling times (τ_s). Data in **B** represents mean ± standard deviation (n = 4).

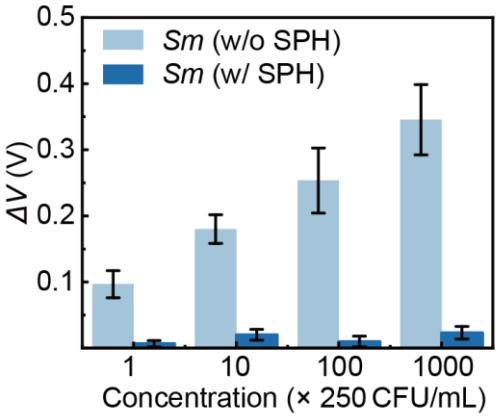


Fig. S9. **Electrical responses of the *Streptococcus mutans* sensor with and without a selective-permeable hydrogel membrane.** The bare sensor without membrane exhibits a strong, concentration-dependent signal in response to *Streptococcus mutans*, indicating direct microbial interaction with the sensing surface. In contrast, the sensor covered with a selective-permeable hydrogel membrane shows significantly attenuated signal intensity, demonstrating the membrane's ability to restrict bacterial penetration and reduce nonspecific interference. Data represents mean ± standard deviation (n = 8).

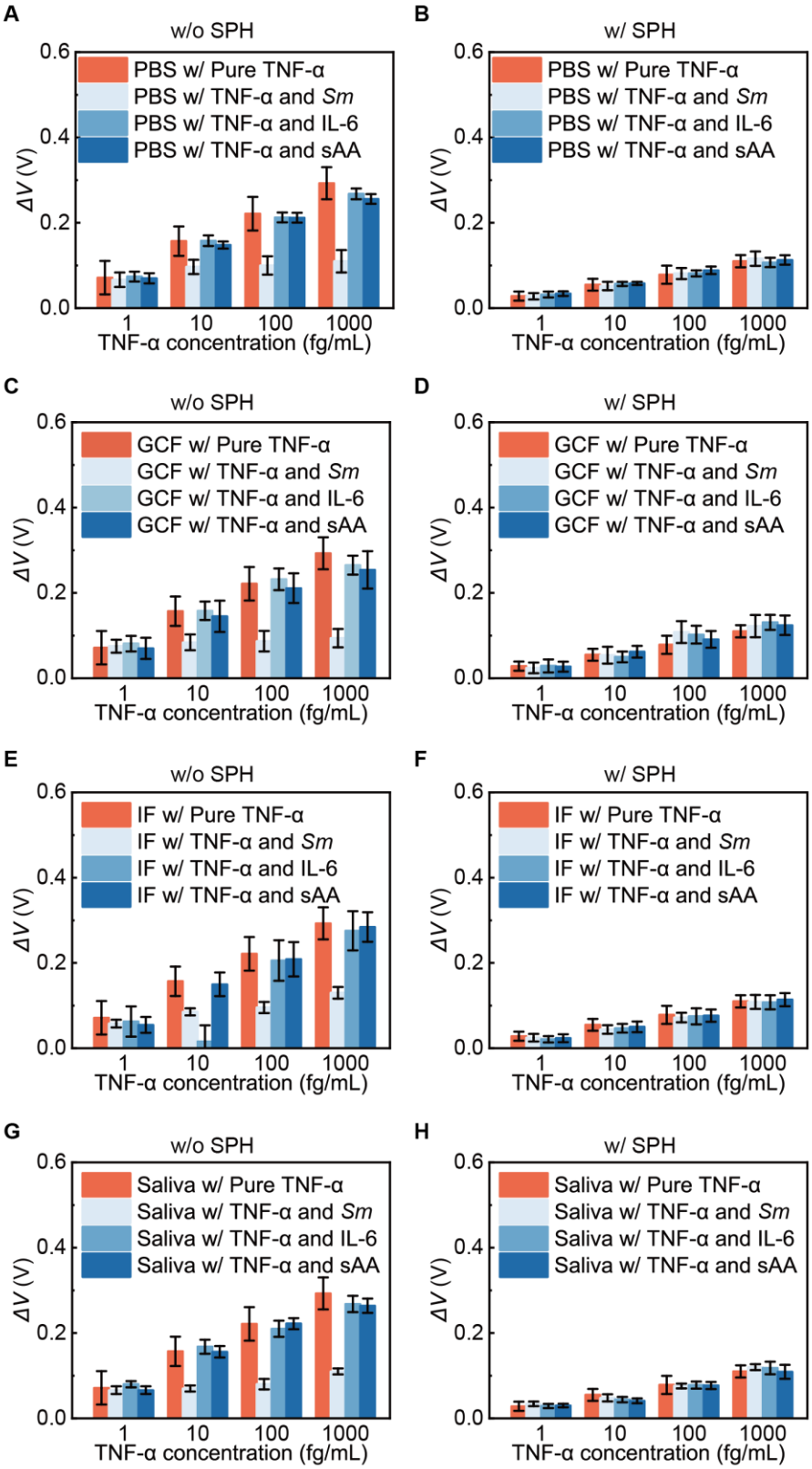


Fig. S10. Dirac point shifts (ΔV) of TAHM biosensor in heterogeneous fluids with verifying TNF-α concentrations with and without a selective-permeable hydrogel membrane. Dirac

point shifts (ΔV) of TAHM biosensor in artificial fluids including PBS (**A**, **B**), gingival crevicular fluid (GCF) (**C**, **D**), intestinal fluid (IF) (**E**, **F**), and saliva (**G**, **H**) with verifying TNF-α concentrations. The concentration of TNF-a is verified from 1 to 1000 fg/mL, while the non-target biomolecules are fixed as 2.5 $\times 10^5$ CFU/mL for *Sm*, 1000 fg/mL for IL-6, and 1000 mU/mL for sAA. Data represents mean ± standard deviation (n = 8).

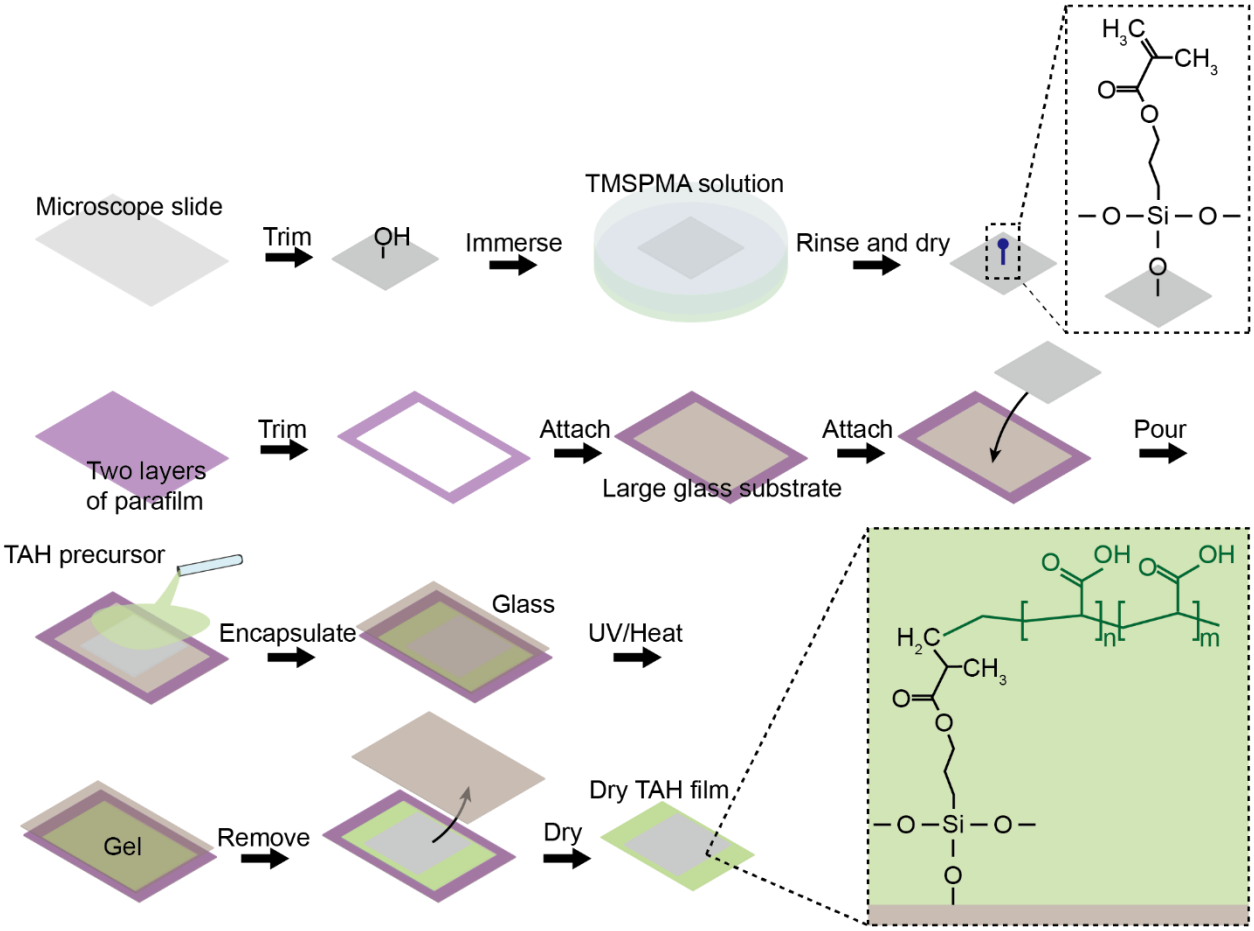


Fig. S11. **Schematic illustration of the fabrication process and adhesion mechanism between the silane-treated glass substrate and the tissue-adhesive hydrogel.** The glass substrate is pre-treated with 3-(trimethoxysilyl)propyl methacrylate (TMSPMA) to introduce methacrylate functional groups on the surface. During hydrogel curing, the acrylate groups within the tissue-adhesive hydrogel precursor undergo free-radical polymerization and form covalent bonds with the silane-modified surface, resulting in strong and stable interfacial adhesion.

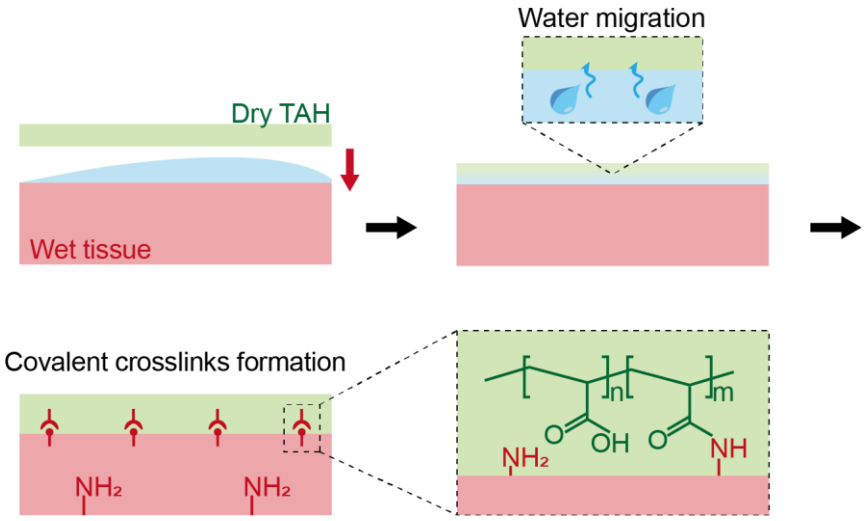


Fig. S12. **Schematic illustration of the adhesion mechanism between the dry tissue-adhesive hydrogel and wet biological tissue.** Upon contact, water molecules from the tissue surface rapidly diffuse into the dry hydrogel, inducing a phase transition from a glassy to a rubbery state. This hydration-driven softening enhances conformal contact. Simultaneously, N-hydroxysuccinimide (NHS) ester groups in the hydrogel react with primary amine groups on the tissue surface, forming covalent amide bonds that establish robust interfacial adhesion.

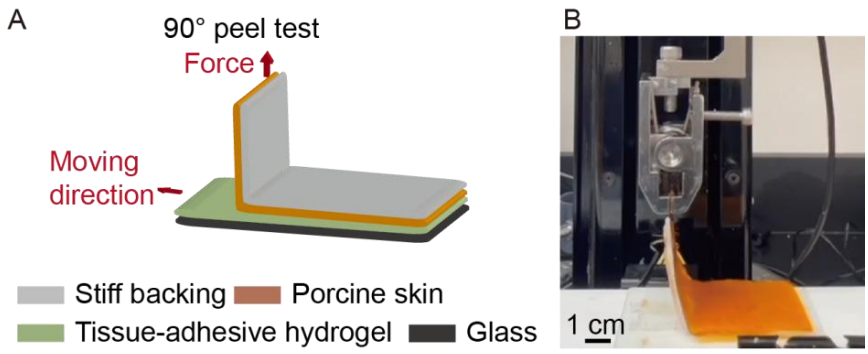


Fig. S13. **90-degree peeling test for evaluating the adhesive performance of the tissue-adhesive hydrogel patch.** (**A**) Schematic illustration and (**B**) corresponding optical image of the 90-degree peeling test setup, in which the tissue-adhesive hydrogel is bonded between a wet biological tissue and a rigid glass substrate.

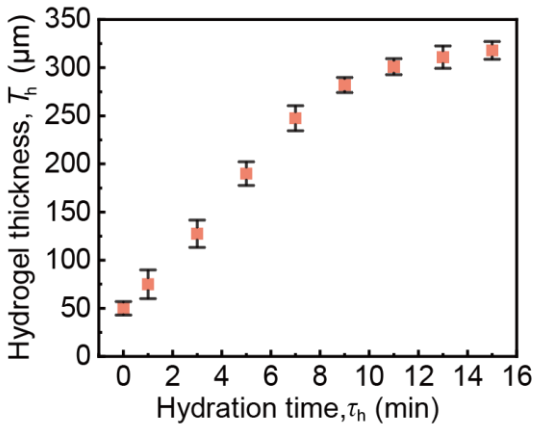


Fig. S14. **Swelling behavior of the tissue-adhesive hydrogel as a function of hydration time.** The thickness of the dry hydrogel patch progressively increases with prolonged hydration, indicating water uptake and swelling. This time-dependent expansion reflects the phase transition from a glassy to a rubbery state and is a critical factor influencing adhesive performance during tissue contact.

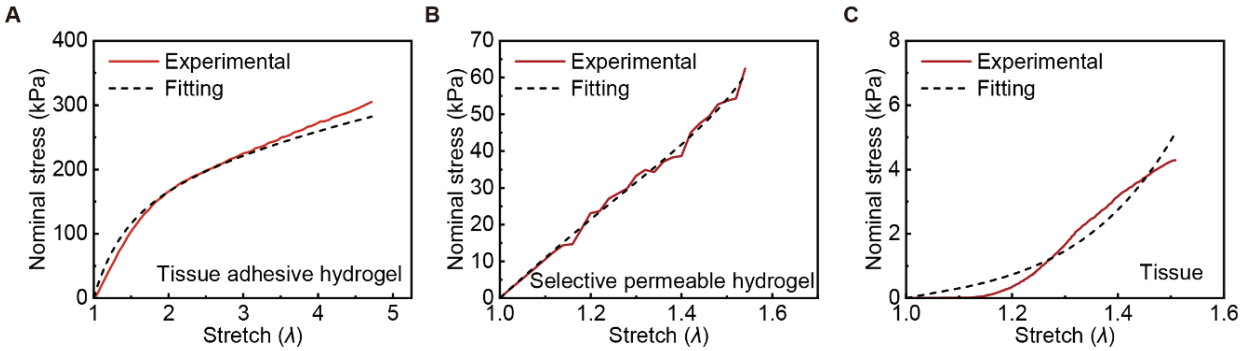


Fig. S15. **Extraction of material parameters from the measured stress-stretch curves for finite element analysis.** (**A**) Tissue-adhesive hydrogel, (**B**) selective-permeable hydrogel, and (**C**) biological tissue. The measured nominal stress verses stretch curves are measured under pure shear tensile loading.

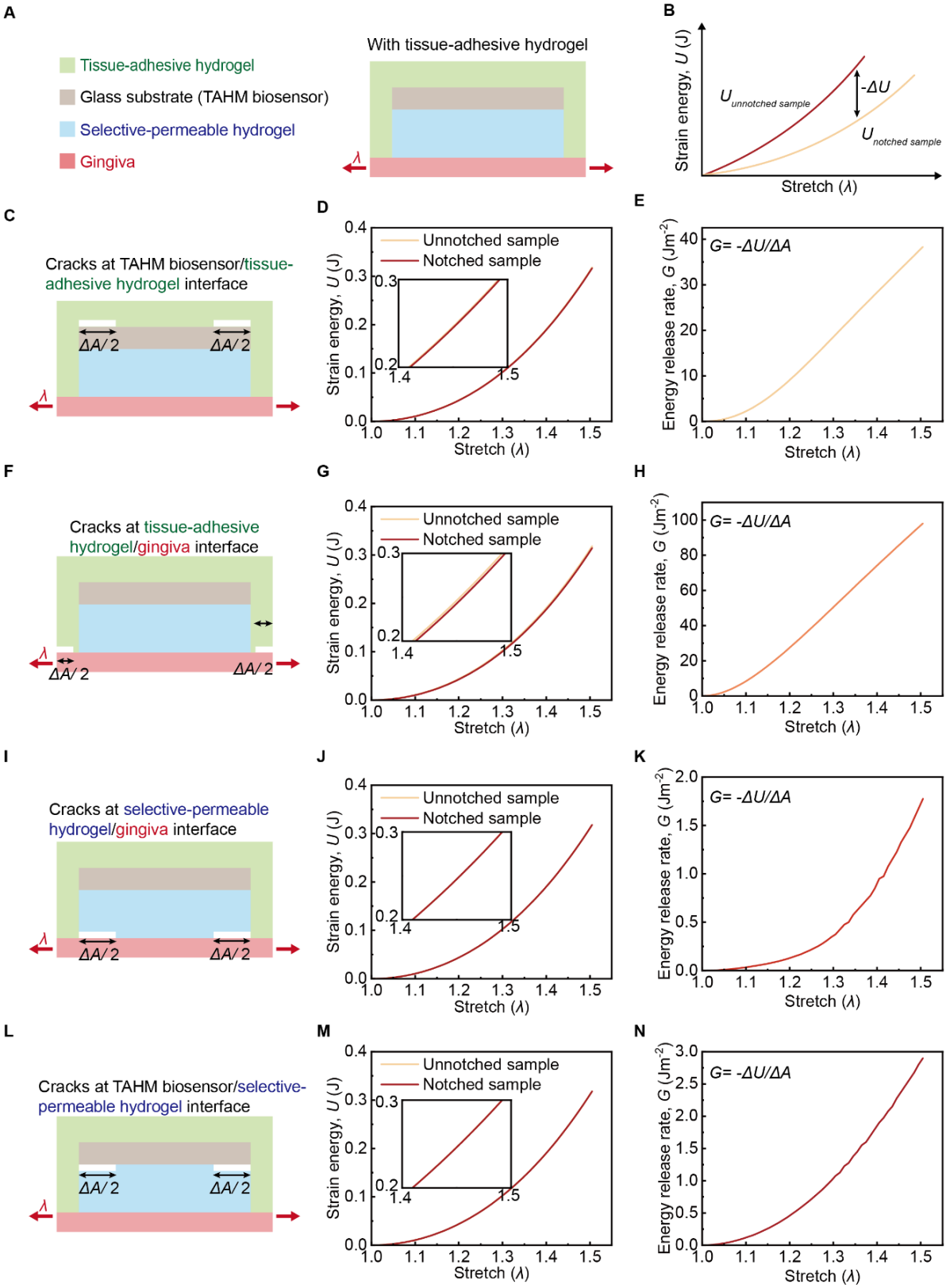


Fig. S16. Finite element modeling of interfacial failure in the TAHM biosensor under tensile deformation. (**A**) Schematic of the TAHM biosensor adhered to a tissue surface via the tissue-

adhesive hydrogel under stretching. (**B**) Illustration of the methodology for calculating strain energy (U) and energy release rate (G) as cracks propagate along different interfaces. (**C–E**) Simulation of crack propagation at the glass/tissue-adhesive hydrogel interface, with corresponding plots of strain energy (**D**) and energy release rate (**E**) as functions of applied stretch. (**F–H**) Simulation of crack propagation at the tissue-adhesive hydrogel/tissue interface, with corresponding strain energy (**G**) and energy release rate (**H**) plots. (**I–K**) Simulation of crack propagation at the selective-permeable hydrogel/tissue interface, with associated strain energy (**J**) and energy release rate (**K**) results. (**L–N**) Simulation of crack propagation at the glass/selective-permeable hydrogel interface, with the corresponding energy plots shown in (**M**) and (**N**).

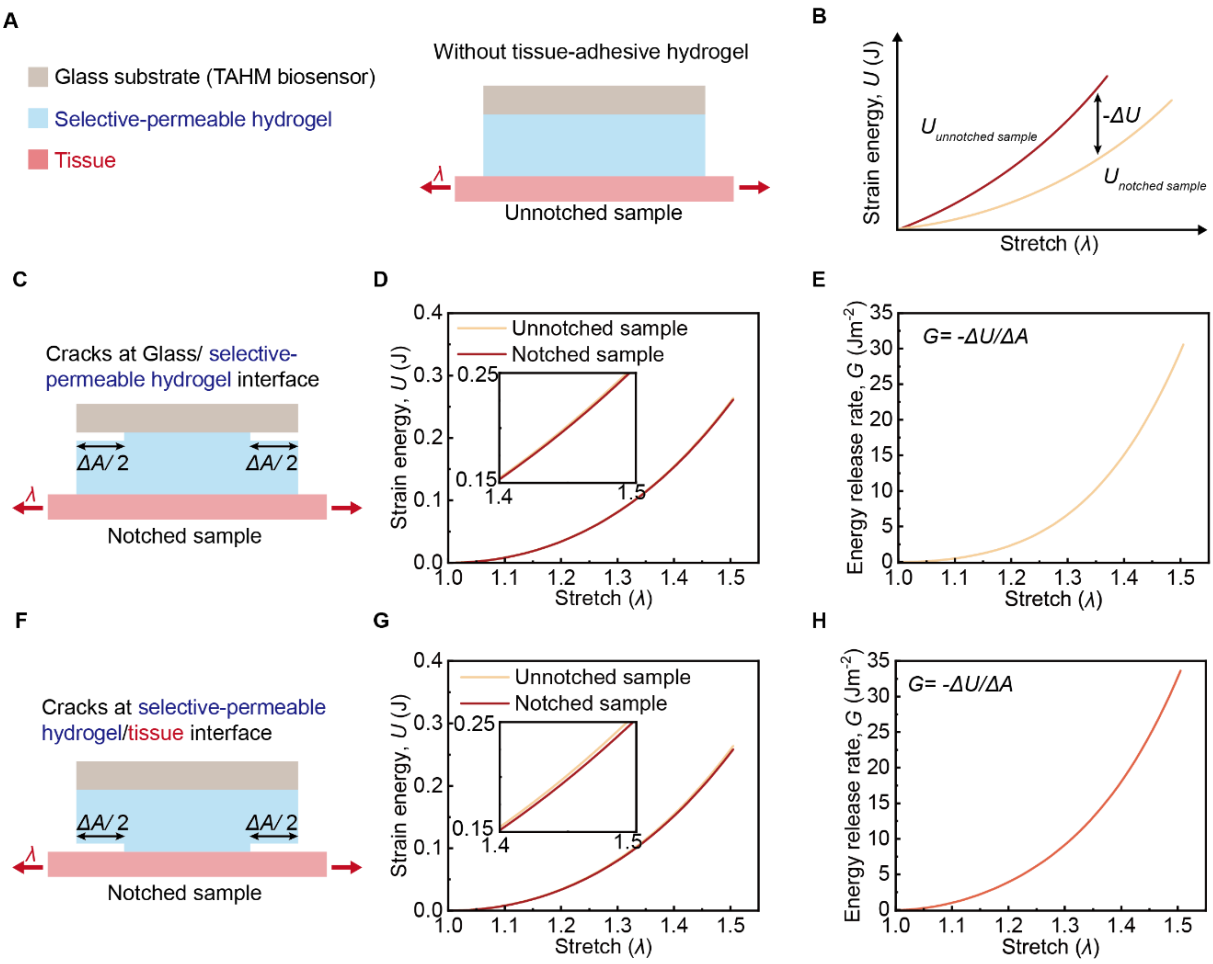


Fig. S17. Finite element modeling of interfacial failure in the TAHM biosensor without a tissue-adhesive hydrogel layer. (**A**) Schematic of the TAHM biosensor directly attached to a tissue surface under tensile deformation, in the absence of a tissue-adhesive hydrogel patch. (**B**) Schematic illustration of the method used to calculate strain energy (*U*) and energy release rate (**G**) during interfacial crack propagation. (**C–E**) Simulation of crack propagation at the glass/selective-permeable hydrogel interface, with corresponding strain energy (**D**) and energy release rate (**E**) plotted as functions of applied stretch. (**F–H**) Simulation of crack propagation at the selective-permeable hydrogel/tissue interface, with corresponding strain energy (**G**) and energy release rate (**H**) data. The results demonstrate significantly higher energy release rates compared to interfacial toughness in the absence of adhesive hydrogel support, indicating increased risk of delamination under mechanical stress.

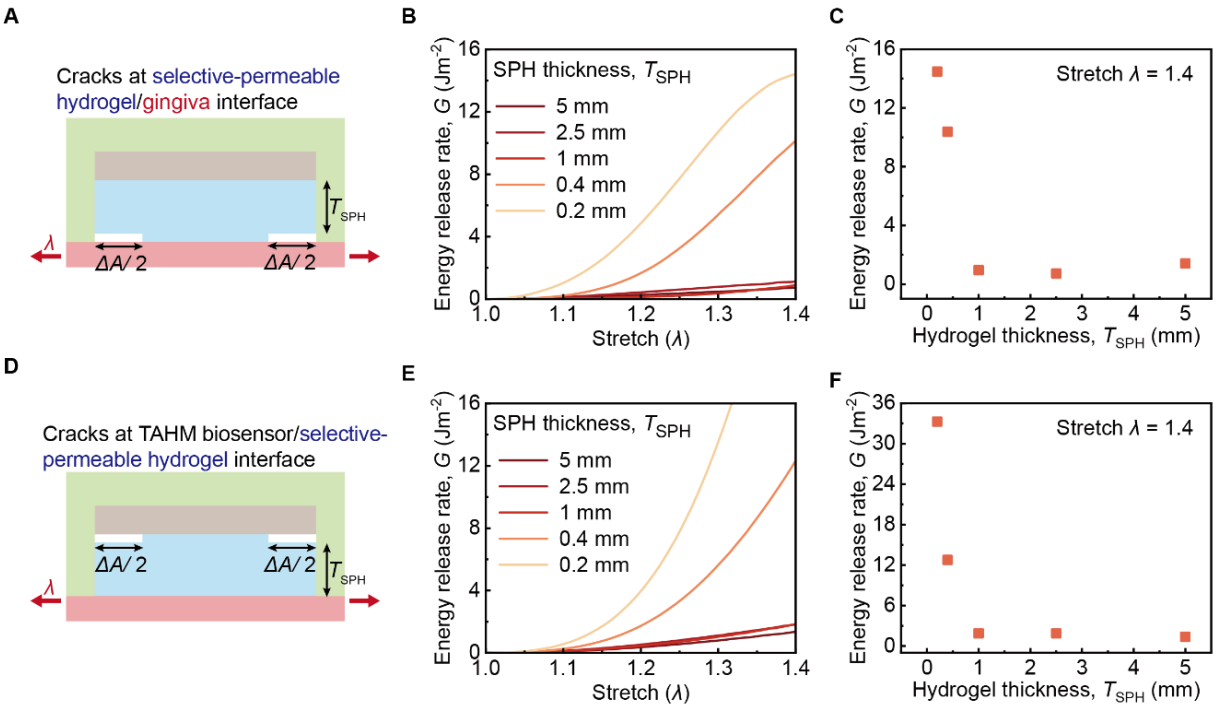


Fig. S18. **Finite element modeling of interfacial failure in the TAHM biosensor with various SPH thicknesses under tensile deformation**. (**A**) Simulated crack propagation at the SPH/tissue interface with varying SPH membrane thicknesses (T_{SPH}). (**B**) Corresponding energy release rate profiles as a function of tensile stretch. (**C**) Extracted energy release rate values at a fixed stretch ratio of λ = 1.4, comparing the effect of membrane thickness across interfaces. (**D**) Simulated crack propagation at the SPH/biosensor interface with varying SPH membrane thicknesses (T_{SPH}). (**E**) Corresponding energy release rate profiles as a function of tensile stretch. (**F**) Extracted energy release rate values at a fixed stretch ratio of λ = 1.4, comparing the effect of membrane thickness across interfaces.

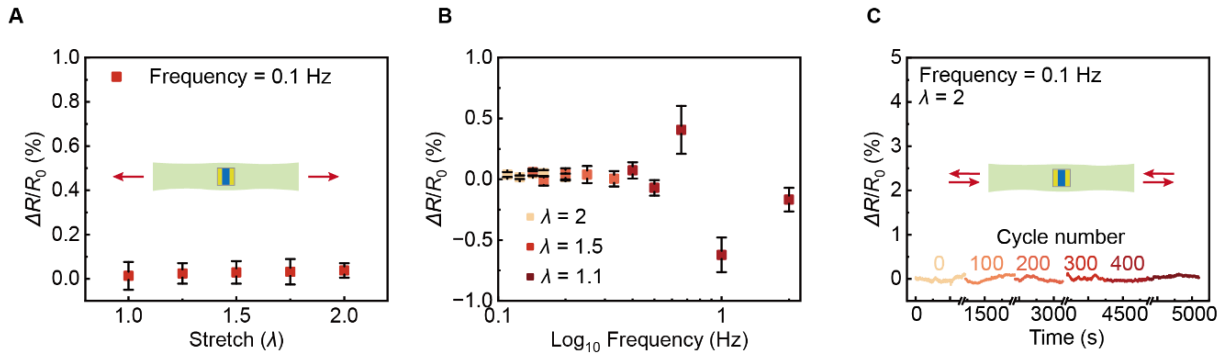


Fig. S19. **Evaluation of strain sensitivity in the TAHM biosensor under varying mechanical conditions.** (**A**) Resistance stability of the biosensor under different stretch levels (λ = 1.0–2.0). (**B**) Sensor response under varying stretching frequencies (0.1–1.5 Hz). (**C**) Signal stability across repeated stretching cycles (up to 500 cycles).

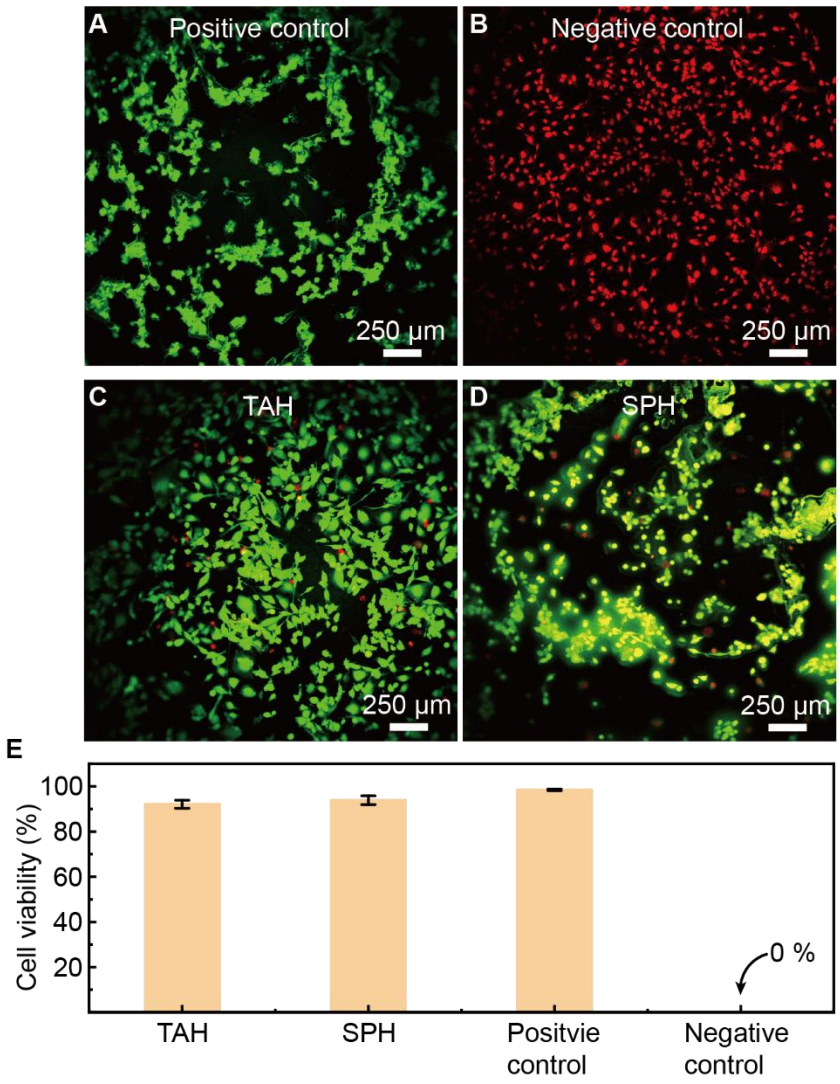


Fig. S20. **Cell viability tests.** Untreated cells serve as the positive control (**A**), while cells treated with 70% ethanol are used as the negative control (**B**). Cell viability after 24 h incubation with medium pre-exposed to the (**C**) tissue-adhesive hydrogel and (**D**) selective-permeable hydrogel. Green fluorescence indicates viable cells, while red indicates dead cells. (**E**) Cell viability of four groups. Data in (**E**) represent mean ± standard deviation (n = 4).

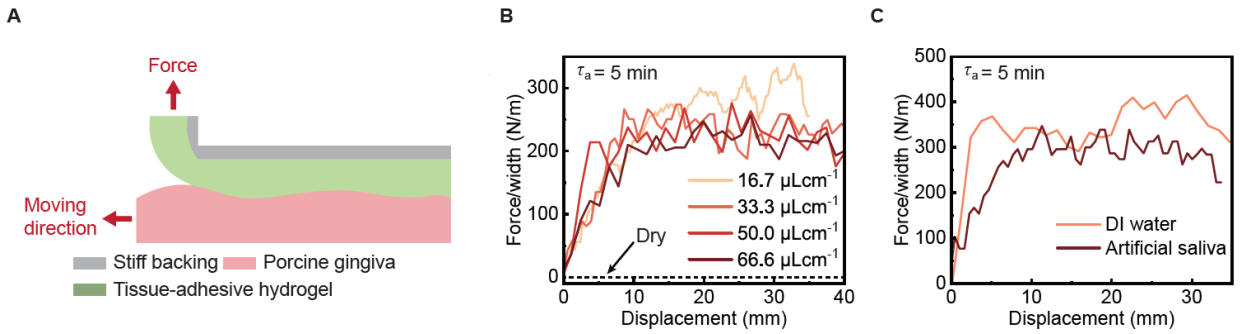


Fig. S21. Adhesion performance of tissue-adhesive hydrogel under various wet conditions. (**A**) Schematic illustration of the 90-degree peeling test used to evaluate the adhesion performance of the tissue-adhesive hydrogel on porcine gingiva. (**B**) Adhesion performance of the tissue-adhesive hydrogel patch on wet porcine skin under varying surface water content. (**C**) Comparison of the adhesion performance of the tissue-adhesive hydrogel patch on wet porcine skin in the presence of DI water versus artificial saliva.

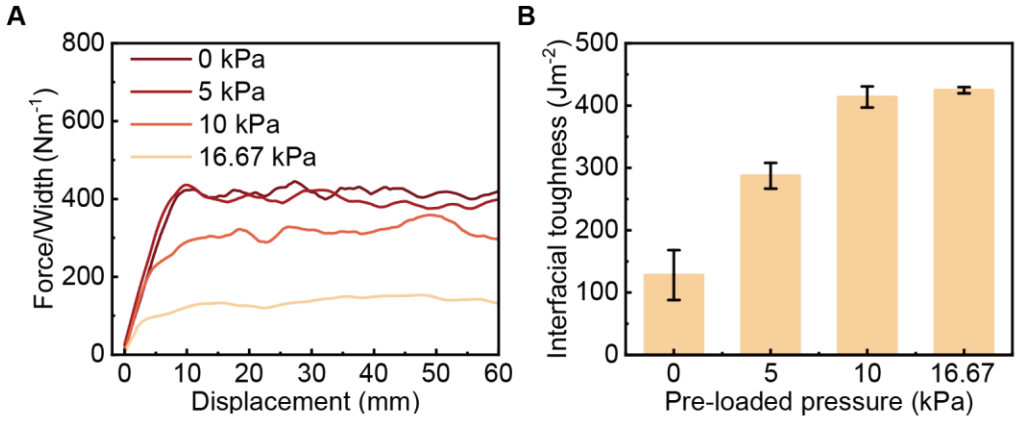


Fig. S22. **Adhesion performance of tissue-adhesive hydrogels under varying pre-loading pressures.** (**A**) Representative force–displacement curves obtained from 90° peel tests under different pre-loading pressures. (**B**) Quantified interfacial toughness of hydrogel patches as a function of pre-loading pressure. Data in (**B**) represent mean ± standard deviation (n = 3).

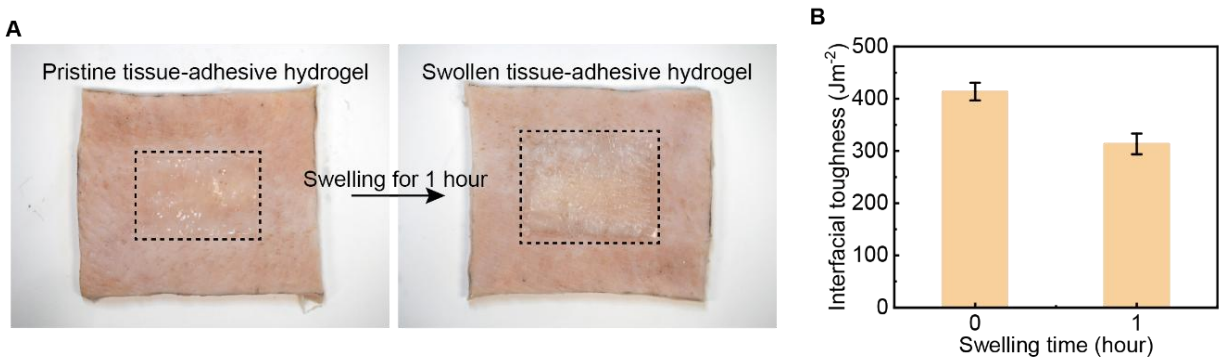


Fig. S23. **Adhesion performance of tissue-adhesive hydrogels before and after swelling.** (**A**) Optical images of a tissue-adhesive hydrogel patch adhered to porcine skin before and after swelling. (**B**) Interfacial toughness of hydrogel patches measured at 0 and 1 hour of swelling. Data in (**B**) represent mean ± standard deviation (n = 3).

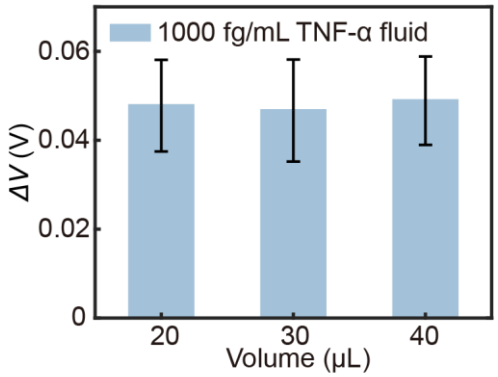


Fig. S24. Signal output of the TAHM biosensor exposed to different fluid volumes. Data are presented as mean ± standard deviation (n = 8).

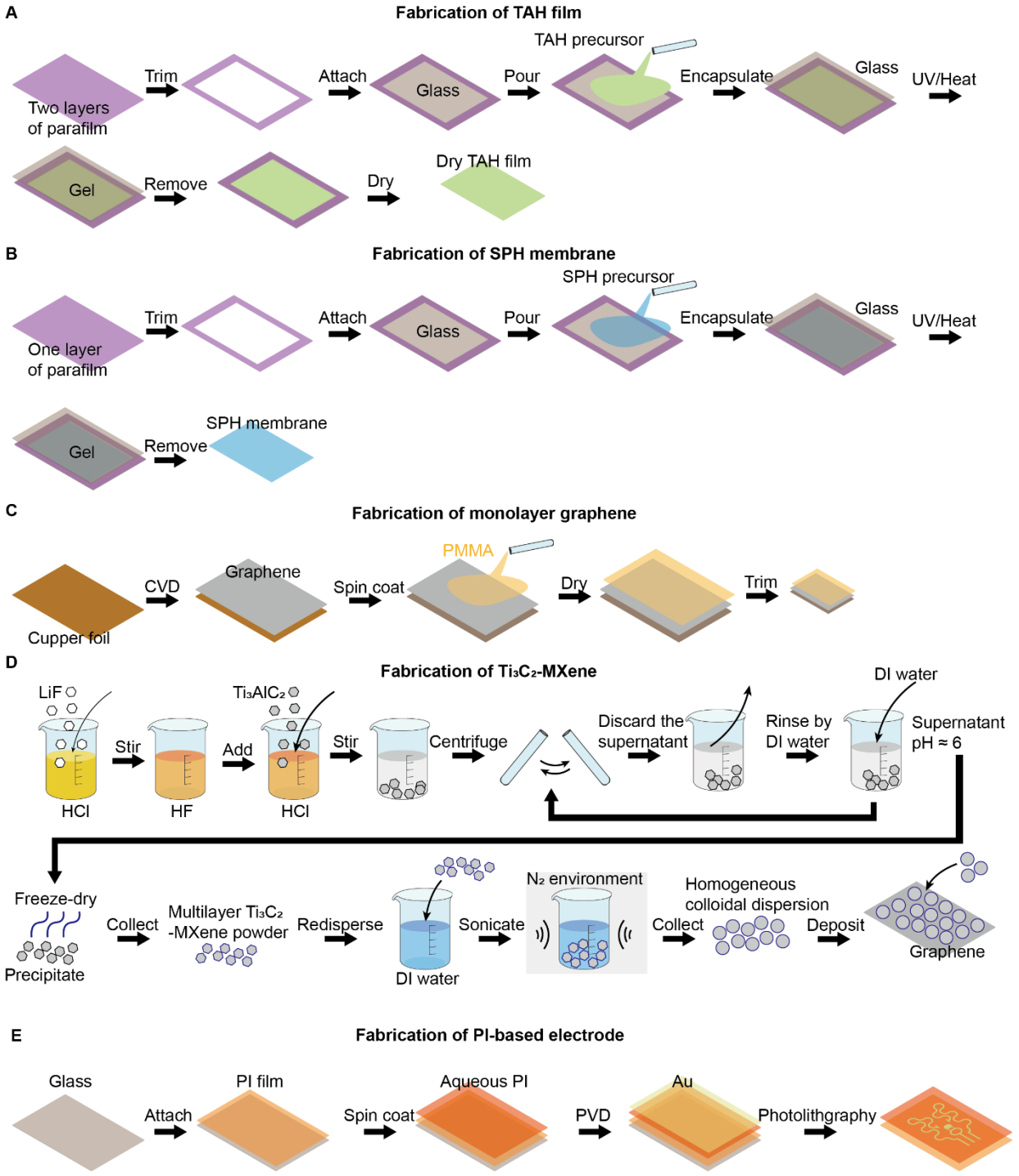


Fig. S25. Schematic illustrations of the surface funcationlaization and assembling processes of the TAHM biosensor. Synthesis flows of tissue-adhesive hydrogel film (**A**) and selective-permeable hydrogel patch (**B**). Fabrication flows of monolayer graphene (**C**), Ti_3C_2-MXene (**D**) and PI-based electrode (**E**).

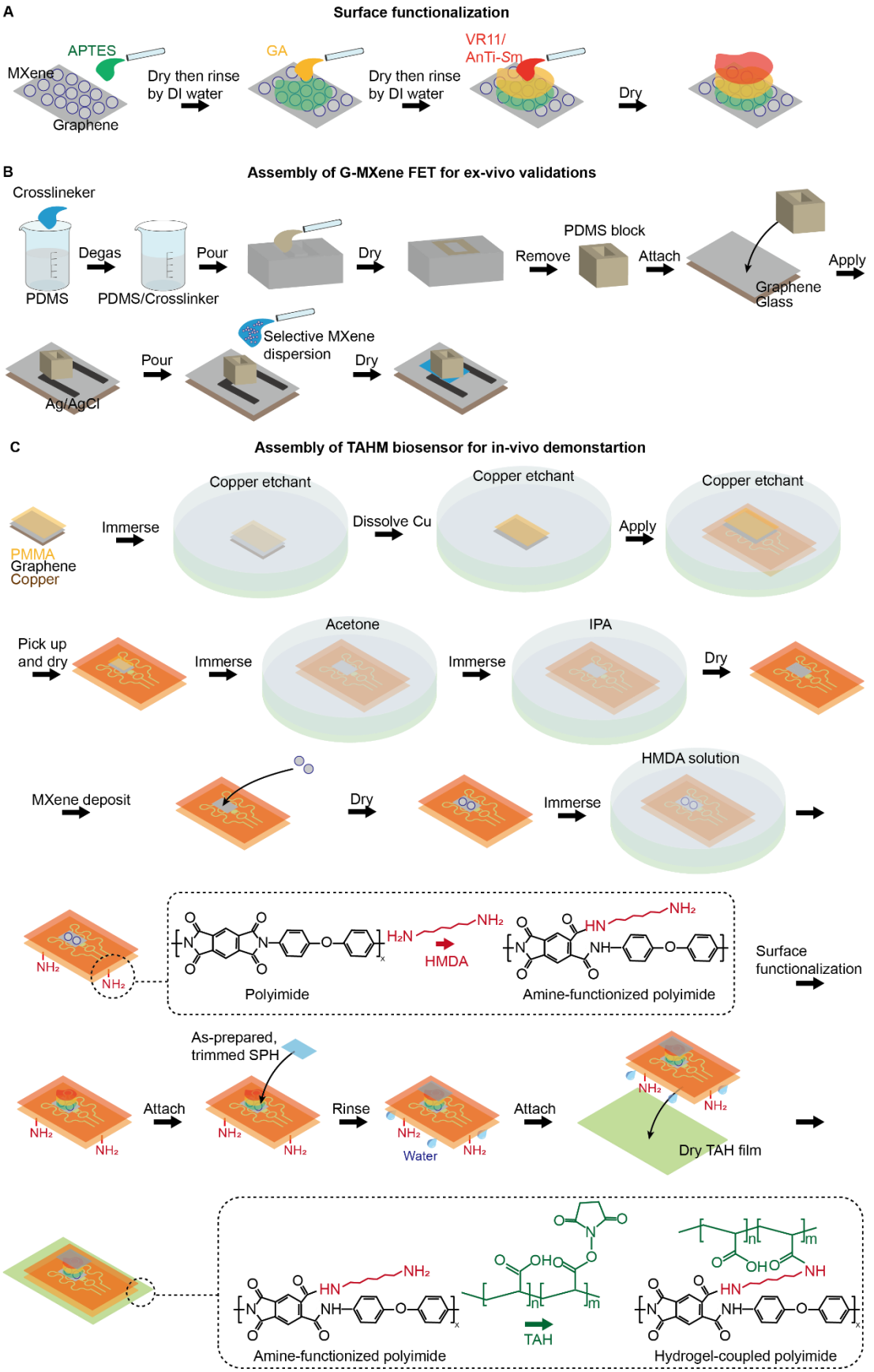

A
Surface functionalization
APTES
MXene
Graphene
Dry then rinse by DI water
GA
Dry then rinse by DI water
VR11/ AnTi-Sm
Dry
B
Assembly of G-MXene FET for ex-vivo validations
Crosslineker
PDMS
Degas
PDMS/Crosslinker
Pour
Dry
PDMS block
Remove
Attach
Graphene
Glass
Apply
Ag/AgCl
Pour
Selective MXene dispersion
Dry
C
Assembly of TAHM biosensor for in-vivo demonstartion
PMMA
Graphene
Copper
Immerse
Copper etchant
Dissolve Cu
Copper etchant
Apply
Copper etchant
Pick up and dry
Immerse
Acetone
Immerse
IPA
Dry
MXene deposit
Dry
Immerse
HMDA solution
NH₂
H₂N
HMDA
Polyimide
Amine-functionized polyimide
Surface functionalization
As-prepared, trimmed SPH
Attach
Rinse
Water
Attach
Dry TAH film
TAH
Amine-functionized polyimide
Hydrogel-coupled polyimide

Fig. S26. Schematic illustrations of the surface funcationlaization and assembling processes of the TAHM biosensor. (**A**) surface funcationlaization of the biosensor. Assembling pricess for G/MXene FET for ex-vivo validations (**B**), and the TAHM biosensor for in-vivo demonstartion (**C**).

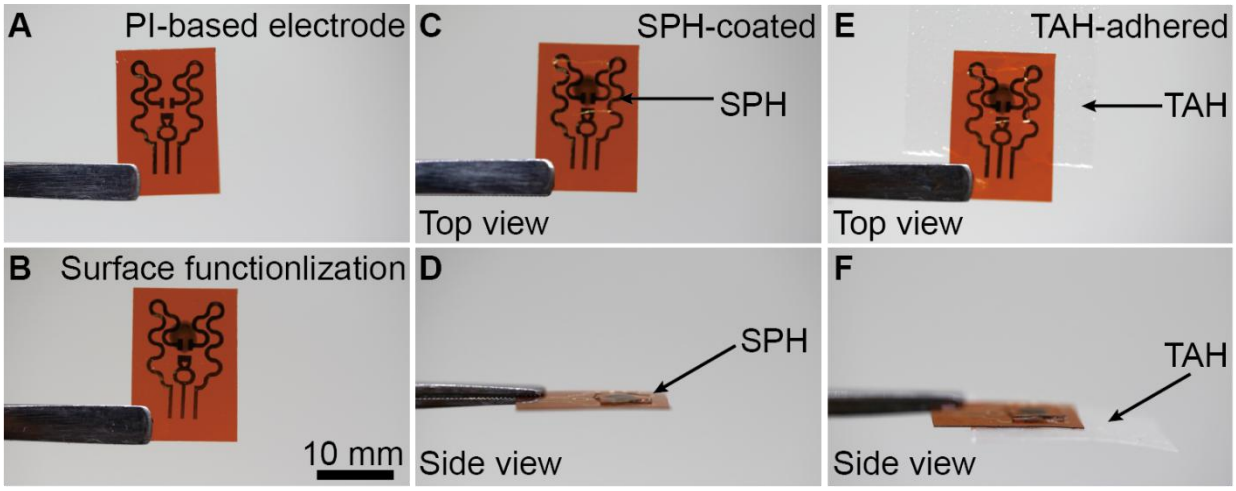


Fig. S27. Optical images of the TAHM biosensor. (**A**) Bare PI-based electrode. (**B**) Electrode after surface functionalization. (**C**, **D**) Top and side views of the electrode coated with a SPH membrane. (**E**, **F**) Top and side views of the electrode adhered to a TAH patch.

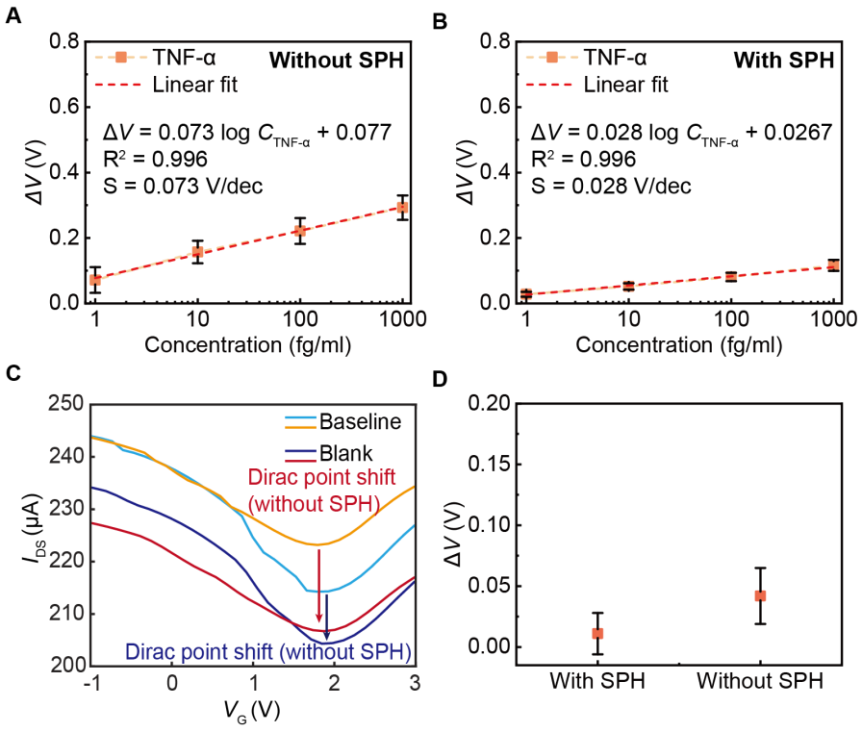


Fig. S28. Supplementary data for the LOD determination of the TAHM biosensor. (**A**, **B**) Calibration curves for TNF-α detection without (**A**) and with (**B**) the SPH, showing the linear regression with the slope (*S*) and intercept (*b*). (**C**) Representative response curves of the baseline and the blank solution for sensors with and without the SPH. (**D**) Average Dirac point shifts and corresponding standard deviations. Data in (**A**), (**B**), and (**D**) are presented as mean ± standard deviation (n = 8).

Table S1. Comparison between our TAHM biosensor and reported field effect transistors.

No	Target biomolecule	Material	Specificity/ Selectivity	Limit of detection (LOD) (fg/mL)	Lowest concentration detected (fg/mL)	Ref.
1.	TNF-α	Graphene/MXene	Aptamer	2.9 (without SPH), 18.2 (with SPH)	1	This work
2	TNF-α	MoS_2	Antibody	fM level	1000	(22)
3	IL-1β	MoS_2	Antibody	fM level	17.5	(23)
4	IL-1β	MoS_2	Antibody	250	100	(24)
5	IL-6	PQDs, SLG, AuNP	Antibody	0.9	1	(25)
6	IL-6	MXene	Aptamer	2.34	10	(26)
7	IL-4, IL-2	Si nanowires	Aptamer	45-75	25	(27)
8	IL-6	Interdigitated electrode, streptavidin	Aptamer	210	21	(28)

Table S2. Comparison between our TAHM biosensor and reported TNF-α biosensors.

No	Target biofluid	Experiment type	Limit of detection (LOD) (fg/mL)	Detection time	Specificity/ Selectivity	Specificity (mixed fluid)	Stability	Ref.
1.	Oral excretion	In vitro, In-situ, ex vivo	2.9 (without SPH), 18.2 (with SPH)	20 min	Aptamer, hydrogel	Specific to TNF -α, below 7% in mixed fluids	Below 0.5 %	This work
2	Serum	In vitro	550	NA	TNF-α template	Specific to TNF -α	NA	(49)
3	Artificial tears, sweat, saliva	In vitro, ex vivo	24.1	7 min	Aptamer	Specific to TNF -α	NA	(50)
4	Sweat	In vitro, In-situ, ex vivo	530	NA	Aptamer	Specific to TNF -α	3.8-5.4 %	(51)
5	Artificial sweat	In vitro, ex vivo	2200	NA	Aptamer	Specific to TNF -α	NA	(52)
6	Sweat	In vitro, In-situ, ex vivo	170	NA	Aptamer	Specific to TNF -α	5 %	(53)

Movie S1. Finite element analysis (FEA) of stretching a TAHM biosensor with tissue-adhesive hydrogel.

Movie S2. Finite element analysis (FEA) of stretching a TAHM biosensor without tissue-adhesive hydrogel.

Movie S3. In vivo characterization of the TAHM biosensor using an anesthetized guinea pig as the animal model.